PAPER

Enhancement of torque density and power density of polymer-based ultrasonic motors via flexible usage of anisotropy in elastic property

To cite this article: Jinshuo Liu *et al* 2023 *Smart Mater. Struct.* **32** 075020

View the article online for updates and enhancements.

You may also like

- A Hierarchical Point-spread Function Reconstruction Method
  Pedro Alonso, Jun Zhang and Cong Liu

- Moisture and temperature influence on mechanical behavior of PPS/buckypapers carbon fiber laminates
  J A Rojas, L F P Santos, M L Costa et al.

- Simulating the replication and entanglement of semi-rigid polymers in nano-injection moulding
  Yuanqi Jiao and Wenshi Ma

Enhancement of torque density and power density of polymer-based ultrasonic motors via flexible usage of anisotropy in elastic property

Jinshuo Liu[1], Jiang Wu[1,*] ⓘ, Xing Gao[2], Zhaochun Ding[1] ⓘ and Wentao Wei[2]

[1] School of Control Science and Technology, Shandong University, Jinan 250061, People's Republic of China
[2] School of Mechanical Engineering, Shandong University, Jinan 250061, People's Republic of China

E-mail: wujiang@sdu.edu.cn

Abstract

The carbon-fiber-reinforced poly phenylene sulfide (PPS/CF), which exhibits low density, low energy dissipation, and relatively high elastic modulus among polymers, is a promising material as the vibrating body of lightweight ultrasonic motors (USMs). Interestingly, the flexible usage of the anisotropy in PPS/CF's elastic property (induced by carbon fibers' reinforcement) offers a new idea to enhance the torque densities and power densities of the polymer-based USMs. As the key issue of flexibly using the anisotropy, this study aims to accomplish the optimal arrangement of the carbon-fibers' filling direction according to the structure, the vibration mode, and the piezoelectric material's polarization direction of the PPS/CF-based motor by performing model construction, structural optimization, and experimental verification. Initially, the dynamic model capable of setting PPS/CF's anisotropically elastic moduli with the changeable filling direction is established to analyze the vibration characteristics. Subsequently, to increase the vibration velocity, the stiffness, and the electromechanical coupling factors, the optimization is carried out for the PPS/CF-based ring-shaped vibrators, where the optimal angle between the filling direction and the vibrator's bottom surface is estimated as 60°. Finally, a prototype of the PPS/CF-based vibrator 30 mm in diameter and 8.5 mm in height is fabricated to form a rotary motor, whose movement and load characteristics are investigated through experiments. At 250 V voltage and 24.42 kHz frequency, the motor yields the no-load rotation speed, the maximal torque, and the maximal output power of 99.3 r min^{-1}, 29.8 mNm, and 72 mW, respectively. Moreover, its torque density and power density reach respectively 7.1 Nm kg^{-1} and 17.1 W kg^{-1}, relatively high among the rotary motors with polymer vibrating bodies. This study validates the effectiveness of our idea and also provides a basic approach to design lightweight USMs that employ newly-developed materials with anisotropically elastic properties and good vibration characteristics.

Keywords: polymer-based ultrasonic motor, carbon-fiber-reinforced poly phenylene sulfide, anisotropically elastic modulus, torque density, power density

(Some figures may appear in colour only in the online journal)

* Author to whom any correspondence should be addressed.

1. Introduction

Ultrasonic motors (USMs) generate mechanical vibration based on inverse piezoelectric effect [1], achieve the actuation via frictional force between the vibrators and rotors/sliders [2], and convert electrical signals into rotary/translational movement [3]. Compared to electromagnetic motors, USMs offer simple structures, self-locking at power-off stage, and no electromagnetic interference [1, 3]. In recent years, rotary USMs have attracted much attention since their compact structures make them potentially applicable to some special application areas [4–6], e.g. optical precision platforms [7, 8], surgical devices [9–11], or micro-/meso-sized telescopes [10, 12, 13]. However, it has still been an important issue to enhance torque densities and/or power densities of rotary USMs as it contributes to realizing lightweight and good controllability of entire system [14, 15].

To date, three methods have been dominantly adopted to enhance torque densities and/or power densities of USMs, i.e. optimization in structure [16], improvement in frictional conditions [17], and usage of new materials [18]. As the examples of structural optimization [8, 19–22], Chen *et al* [21] attempted to improve the performance by tuning the I-shaped portion's thickness between the teeth's surface and the bonding layer. Zhang *et al* [22] analyzed how the resonance frequencies of both longitudinal and bending vibrations depended on the driving feet's dimensions. As a common problem of optimization, the frequency degeneration is necessarily performed to generate elliptical motions on the driving feet [23, 24]; this makes it not easy to greatly change the vibrators' structure especially when there exists spatial limitation in some fields (e.g. pipe-crawling robots [10] or optical instrument for endoscopic usage [12]). Improvement of the frictional condition can be achieved by utilizing the friction materials [17, 25, 26], modifying the surface morphology [27–29], or using the lubrication [30]. As typical examples, Zhao *et al* [25] used aramid/molybdenum-disulfide composites as the friction materials from the viewpoint that the variation in aramid's glass transition temperature could improve tribological performance of USMs. Li *et al* [27] stated that the wear mechanisms of friction materials sliding against the textured vibrator were mainly caused by the fatigue especially for small-sized friction materials; this provided the criterion to choose USMs' friction materials. Qiu *et al* [30] found that the lubrication with high-traction fluid is helpful to improve USMs' performance owing to the fluid's special capability to reduce friction loss. Though improvement of the frictional condition has been proven as an effective way for certain types of USMs [17], owing to the fact that the vibration characteristics are mainly determined by the vibrators' material properties [1, 8], we still regard that the usage of new materials is prospective for improving USMs' performance [9].

According to the piezoelectricity, the new materials can be applied to USMs as the excitors or vibrating bodies, which have the functions of generation or enlargement of the vibration, respectively. Recent years have witnessed the development of quite a lot of new piezoelectric materials [2, 3]. For instance, Doshida *et al* [31] examined the vibration properties of crystal-oriented piezoelectric ceramics and preliminarily investigated its application to a rotary USM. Gao *et al* [32] used a transparent relaxer ferroelectric crystal to fabricate an L-shaped vibrator capable of translationally walking on the glass platform. These new piezoelectric (or ferroelectric) materials enrich the candidate materials as the excitors, but their vibration properties are mostly inferior to the lead zirconate titanic (PZT) ceramics mainly because of the unique crystal structure of PZT [32]. The vibrating bodies can gather the resonance frequencies of the vibration modes [11], enlarge the vibration amplitude [19], and form the elliptical motions [1], so it is worthwhile to carefully choose the materials for the vibrating bodies. Metal, ceramic, and polymer are the commonly-used engineering materials [9]. Despite the heavy usage in conventional USMs [1, 3], metals' large densities should be the main limitation for further enhancement in torque densities and/or power densities of USMs [33, 34]. Fine ceramics (e.g. alumina or silicon carbide) enable the vibrators to generate large driving force owing to their high rigidity, but fine-ceramics-based USM faces the problem of easy fracture because of the fragility [35]. Compared to metals and fine ceramics, polymers show relatively high applicability owing to their lower densities [36, 37]. Excitingly, our group has found that poly phenylene sulfide (PPS) possesses low energy dissipation due to its semi-crystalline molecular structure (see figure 1(a)) and confirmed the feasibility to employ PPS as the vibrating bodies of USMs [38–40]. However, the low elastic modulus of PPS causes the mismatching in acoustic impedances between the PPS vibrating bodies and the PZT plate [39, 41], so it is still required to enhance torque density and/or power density of polymer-based rotary USMs, where a candidate method is that the vibrating body is formed with 'rigid' PPS.

By inserting long carbon fibers into PPS with the pultrusion process [42], Toray Corporation has invented a new composite, i.e. carbon-fiber-reinforced PPS (referred to as PPS/CF). Interestingly, the carbon fibers' reinforcement increases the rigidity along the filling direction [42]. More importantly, PPS/CF inherits low density and low energy dissipation as its basic matrix is still PPS [38, 42–44]. Our former study [43] validates that these properties exactly mitigate the shortcoming of the insufficient rigidity of conventional PPS (see figure 1(b)). The carbon fibers' reinforcement leads to the anisotropy in PPS/CF's elastic moduli, which are commonly undesirable as it makes the vibration complicated. However, on condition that the carbon fibers' filling direction is arranged optimally, the relatively high elastic modulus possibly improves the impedance matching and consequently increase the driving force of the PPS/CF-based vibrator, and meanwhile, the relatively low elastic moduli in the other directions likely suppress excessive reductions in the vibration velocity. Thus, the flexible usage of anisotropy in PPS/CF's elastic property offers a new idea to enhance the actuating capability of the PPS/CF-based vibrators.
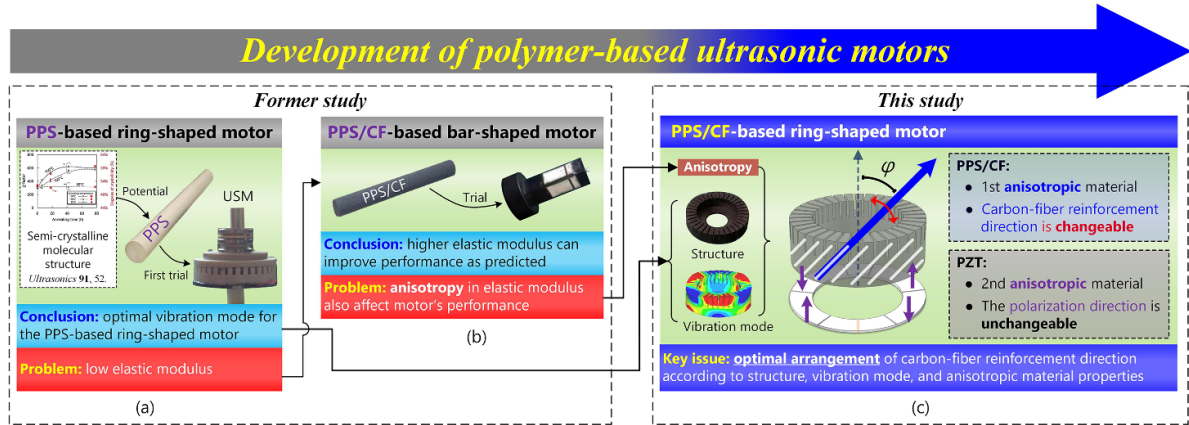
Figure 1. Development of the polymer-based USMs. (a) The initial step of the PPS-based motor, indicating the feasibility of applying polymer to USMs. (b) The following trial of the PPS/CF-based motor, implying the positive effect due to the relatively elastic modulus of PPS/CF. (c) This trail, aiming at the flexible usage of the anisotropy in PPS/CF's elastic property.

In this study, we test whether the variation of the carbon fibers' filling direction can enhance the torque densities and/or power densities of the polymer-based rotary USMs. In contrast to the previous studies that only regard the PZT plates' anisotropy [9, 10, 16], this study aims to optimally arrange the carbon-fibers' filling direction by considering the anisotropy in both the vibrating body and the PZT plate (see figure 1(c)); this is, to the best of our knowledge, the first trial in the field of USMs. Here, the PPS/CF-based motor works in the 3rd-bending and 1st-longitudinal hybrid modes and has the ring shape, though both of which have been adopted in previously-reported USMs, their capability to avoid the frequency degeneration makes it easy to design the vibrators [9] and allows us to better understand the positive effect induced by the flexible usage of anisotropy. Besides, the PPS/CF vibrating bodies with different filling direction are fabricated by simply changing the cutting directions (see Section 3); this avoids the special manufacturing of the PPS/CF samples with various filling directions and consequently decreases the expense (which is not more than 40 dollars for each vibrator including the PPS/CF vibrating body and the multi-polarized PZT plate).

This paper presents the proposal, design, and performance assessment of the PPS/CF-based motors, and its main contributions are as follows.

(1) An FEA-based dynamic model capable of setting the anisotropic elastic moduli with changeable filling directions is constructed as a practical tool to analyze the dynamic parameters of the PPS/CF-based vibrators.
(2) The relationships between the filling angles and the dynamic parameters (including the vibration velocities, equivalent stiffnesses, and electromechanical coupling factors) were clarified to provide the theoretical basis for structural optimization.

The rest of this paper are organized as follows. Section 2 designs the dynamic model and conducts optimization of the

PPS/CF-based vibrators. Sections 3 and 4 demonstrate the vibration properties and movement/load characteristics of the PPS/CF-based motors. Section 5 concludes this paper.

2. Design of PPS/CF-based vibrators

2.1. Configuration and vibration mode

Figure 2(a) schematically depicts the vibrator, consisting of a PPS/CF vibrating body and a ring-shaped PZT plate. The vibrating body is in cylindrical shape and has the diameter of 30 mm, while the back surface is a 0.5 mm-thick disk. A small hole is created in the central position of the disk to fix the vibrator. Many teeth with the intervals of 10° are cut on the cylindrical part to enlarge the vibration amplitude. The teeth's heights are 4 mm and the slots between the adjacent teeth are 0.5 mm. The rotor is in contact with the outer edge of the upper surface. Here, considering that the filling angle (φ) (referred to as the angle between the carbon fiber's filling direction and the r axis) as well as the unslotted-part's thickness (h) mainly affected the vibration properties [44], we regarded φ and h as the key parameters in this study. The PZT plate (P4, Hongsheng Acoust. Corp., Baoding, China) is 30 mm in outer diameter, 20 mm in inner diameter, and 0.5 mm in thickness and bonded onto the PPS/CF vibrating body's back surface. As shown in figure 2(b), the PZT plate is divided into six portions, where four portions with the central angles of 60° are polarized in inverse directions while the other portions are not polarized. When two channels of phased voltages ($V_0 \cdot \cos(2\pi f t)$ and $V_0 \cdot \cos(2\pi f t + \alpha)$, where V_0, f, t, and α are the driving voltage, frequency, time, and phase, respectively) are applied to the portions with 60° central angles, a traveling wave exists on the upper surface. Figure 2(c) shows the vibration mode utilized in this study, where six vertical nodal lines and one horizontal nodal line demonstrate that the 3rd bending and 1st longitudinal vibrations are excited in the θ and z
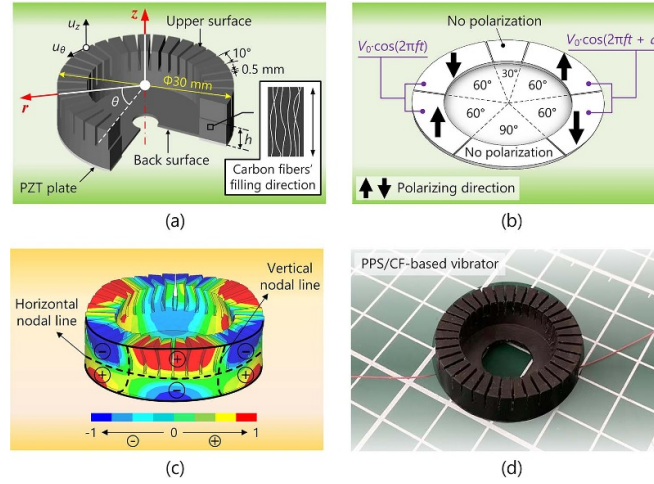
Figure 2. Configuration and the vibration mode of the PPS/CF-based vibrator. (a) illustrates the structure of the vibrator, where the coordinate system (z, θ, and r axes) is established at the upper surface's central position. The θ and z-axis vibration displacements at the edge are expressed as u_θ and u_z, respectively. (b) depicts the PZT plate's polarization. To generate the traveling wave, two groups of electrodes are made on the PZT plate and the annular distance between the two groups (or the unpolarized parts) must be a quarter of wavelength or three quarters of wavelengths [1, 6, 9]. Since the motors work in the 3rd bending mode, a wavelength is equal to 120°, so the unpolarized part corresponds to 30° or 90°. (c) shows the vibration mode, where the legend shows the normalized vibration amplitude. (d) gives the photograph of a prototype of the PPS/CF-based vibrator.

axes; this mode is utilized as our former study [45, 46] has confirmed that, for the polymer-based motors, it provides relatively strong electromechanical coupling compared to conventional bending ones [39]. Figure 2(d) shows the photograph of a prototype of the PPS/CF-based vibrator. Note that the central hole's diameter is slightly larger than that given in the model (see figure 2(a)) as a consequence of fabrication limitation, but it does not markedly change the vibration properties because the part adjacent to the central hole has the 'clamped' boundary condition.

2.2. Dynamic model

Figure 3 illustrates how the dynamic parameters of the PPS/CF vibrators are estimated by combining FEA and the equivalent circuit model. The procedures have two key issues, namely (1) setting the anisotropically elastic moduli and (2) deriving the dynamic parameters.

(1) *Set the anisotropically elastic moduli*. As shown in figure 3(a), the PPS/CF vibrating body and PZT plate are meshed with hexahedral elements. For the PPS/CF vibrating body, the matrix of the elastic moduli corresponding to φ is expressed as [9]

$$\mathbf{E}(\varphi) = \mathbf{M^T}(\varphi) \cdot \mathbf{E} \cdot \mathbf{M}(\varphi). \tag{1}$$

Here, $\mathbf{E}$ denotes the original matrix of PPS/CF's elastic moduli (corresponding to $\varphi = 90°$) [43]:

$$\mathbf{E} = \begin{bmatrix} 11.78 & 2.06 & 9.23 & 0 & 0 & 0 \\ 2.06 & 11.78 & 9.23 & 0 & 0 & 0 \\ 9.23 & 9.23 & 16.14 & 0 & 0 & 0 \\ 0 & 0 & 0 & 3.45 & 0 & 0 \\ 0 & 0 & 0 & 0 & 3.45 & 0 \\ 0 & 0 & 0 & 0 & 0 & 4.86 \end{bmatrix} (\text{GPa}), \tag{2}$$
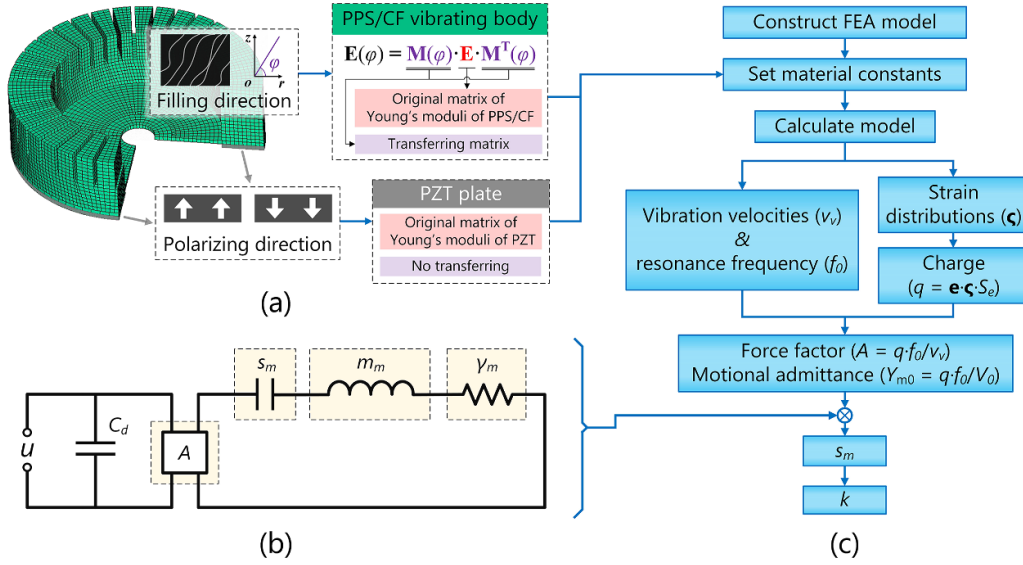
and $\mathbf{M}(\varphi)$ represents the transferring matrix [46]:

$$\mathbf{M}(\varphi) = \begin{bmatrix} \sin^2(\varphi) & 0 & \cos^2(\varphi) & 0 & -\sin(2\varphi) & 0 \\ 0 & 1 & 0 & 0 & 0 & 0 \\ \cos^2(\varphi) & 0 & \sin^2(\varphi) & 0 & \sin(2\varphi) & 0 \\ 0 & 0 & 0 & \sin(\varphi) & 0 & \cos(\varphi) \\ \frac{1}{2}\sin(2\varphi) & 0 & -\frac{1}{2}\sin(2\varphi) & 0 & -\cos(2\varphi) & 0 \\ 0 & 0 & 0 & -\cos(\varphi) & 0 & \sin(\varphi) \end{bmatrix}. \tag{3}$$

Besides, PPS/CF's density is set to 1.69×10^3 kg m^{-3}.

The dielectric, piezoelectric, and elastic matrices of the PZT plate are given as [45]

$$\varepsilon^{\mathbf{S}} = \begin{bmatrix} 15.488 & 0 & 0 \\ 0 & 15.488 & 0 \\ 0 & 0 & 13.010 \end{bmatrix} \times 10^{-9} (\text{Fm}^{-1}), \tag{4}$$

Figure 3. (a) Dynamic model and the method of setting the anisotropically elastic moduli with changeable filling direction of carbon fibers, (b) the equivalent circuit model of the piezoelectric vibrator, and (c) the flowchart of calculating the dynamic parameters from the FEA results.

$$\mathbf{e} = \begin{bmatrix} 0 & 0 & 0 & 0 & 14.0 & 0 \\ 0 & 0 & 0 & 14.0 & 0 & 0 \\ -6.8 & -6.8 & 10.7 & 0 & 0 & 0 \end{bmatrix} \times 10^{-9} \left(\mathrm{C\,m^{-2}} \right),$$

(5)

and

$$\mathbf{c^E} = \begin{bmatrix} 145 & 80 & 84 & 0 & 0 & 0 \\ 80 & 145 & 84 & 0 & 0 & 0 \\ 84 & 84 & 131 & 0 & 0 & 0 \\ 0 & 0 & 0 & 24 & 0 & 0 \\ 0 & 0 & 0 & 0 & 24 & 0 \\ 0 & 0 & 0 & 0 & 0 & 33 \end{bmatrix} (\mathrm{GPa}),$$

(6)

respectively; and its density equals 7.8×10^3 kg m^{-3}. Note that the matric of PZT's elastic moduli are not transferred as PZT's polarizing direction cannot be changed during the fabrication of the PPS/CF-based vibrators [47].

(2) *Derive the dynamic parameters.* As figure 3(b) shows, the equivalent circuit model incorporates an electrical arm and a mechanical arm, coupled with the force factor (A). The mechanical arm comprises three components in series, i.e. the equivalent stiffness s_m, equivalent mass m_m, and equivalent damper γ_m. Here, these parameters can be derived from the FEA results (i.e. the maximal vibration velocity on the upper surface (v_v), resonance frequency (f_0), and strain distribution on electrodes (ς)). First, the clamped capacitance in the electrical arm is expressed as [46, 47]

$$C_d = \varepsilon_{33} S_e / p,$$

(7)

where ε_{33} denotes the dielectric constant in the polarizing direction (13.010×10^{-9} F m^{-1}), S_e represents the electrode's area corresponding to one channel of the driving voltage

(141.8 mm^2), and p means the PZT plate's thickness (0.5 mm). Second, according to the definition of the force factor [9],

$$A = \frac{q \cdot f_0}{v_v} = \frac{\iint (\mathbf{e} \cdot \varsigma) \, dS_e \cdot f_0}{v_v},$$

(8)

where q stands for the strain-induced charge (here, it does not include the charge electrically accumulated on C_d). Besides, through the estimation of the motional admittance ($Y_{m0} = qf_0/V_0$), the equivalent stiffness is derived as [46]

$$s_m = \frac{2\pi f_0 \cdot Q \cdot A^2}{Y_{m0}},$$

(9)

where Q stands for the mechanical quality factor (set to 400 in this study [48]). Third, the electro-mechanical coupling factor is estimated with the following equation [9]:

$$k = \sqrt{\frac{A^2}{A^2 + C_d \cdot s_m}}.$$

(10)

The procedures are listed in figure 3(c), by utilizing which we can obtain the dynamic parameters after carrying out the harmonic analysis.

2.3. Dynamic parameters versus filling direction and key dimension

Prior to structural optimization, it is essential to calculate how φ and h affect v_v, s_m, and k (all of which are the key parameters for USMs) by following the procedures:

(1) Derive the dynamic parameters as φ and h are varied by utilizing the aforementioned dynamic model.

(2) Implement the interpolation with the discrete results to obtain the relationship between the dynamic parameters and the dimensions.
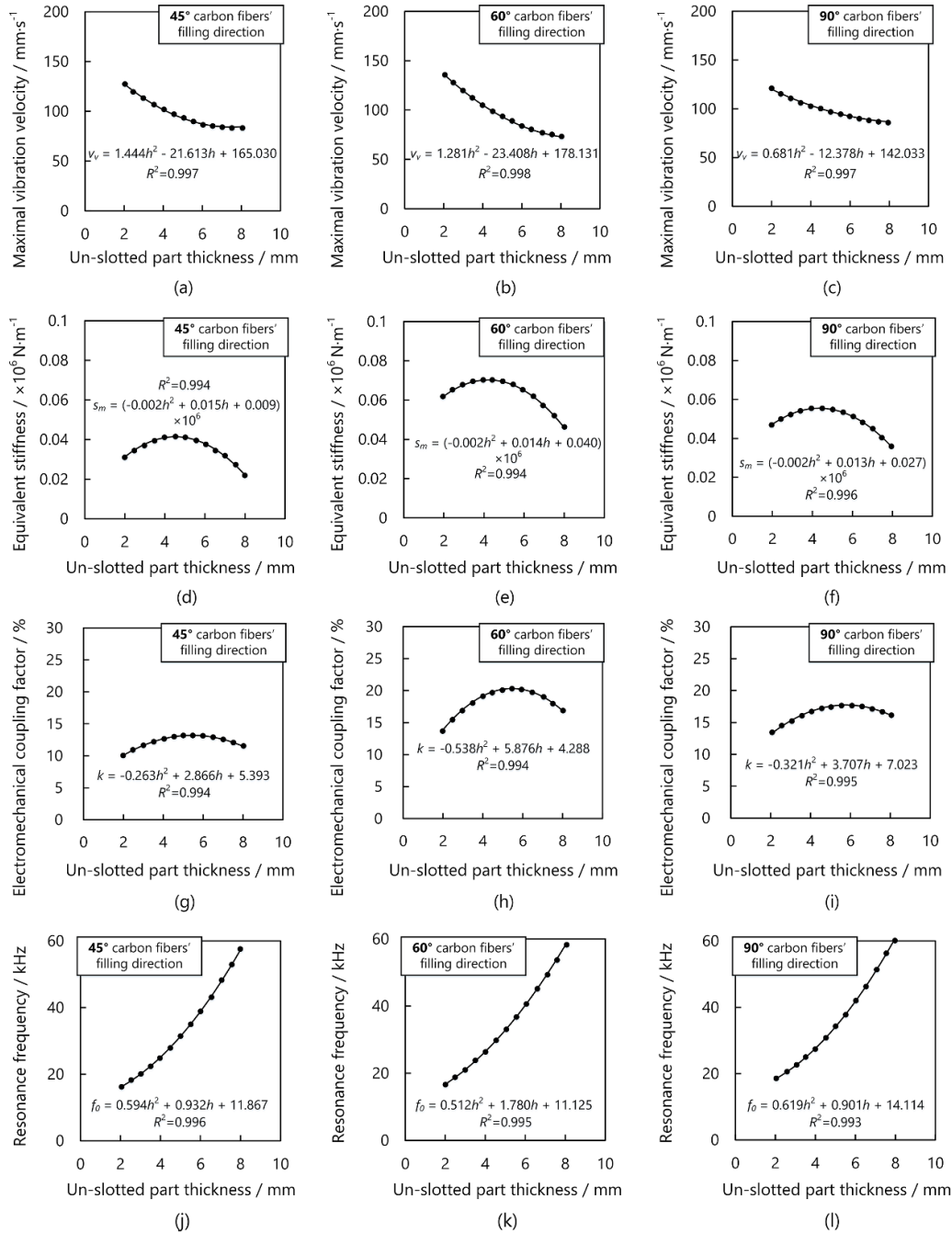
Figure 4. Maximal vibration velocities as functions of h when φ equals (a) $45°$, (b) $60°$, and (c) $90°$. The equivalent stiffness versus h at φ of (d) $45°$, (e) $60°$, (f) $90°$. The variation in electromechanical coupling factor against h when φ is (g) $45°$, (h) $60°$, (i) $90°$. The resonance frequency as functions of h at φ of (a) $45°$, (b) $60°$, and (c) $90°$.

Figure 4(a) shows that, at $\varphi = 45°$, v_v decreases from 127.7 to 84.4 mm s^{-1} as h increased from 2 to 8 mm because the vibrator's stiffness becomes higher. Figures 4(b) and (c) show that almost the same tendencies can be found at $\varphi = 60°$ and $90°$. As for the dependence of s_m on h and φ, it can be observed in figure 4(d) that, at $\varphi = 45°$, s_m increased from 0.031×10^6 to 0.041×10^6 N m^{-1} when h ranged from 2 to 4 mm, and then, s_m decreased to 0.022×10^6 N m^{-1} when h increased to 8 mm probably because of the changes in vibration modes [46]. Figures 4(e) and (f) have the similar tendencies with that in figure 4(d), but the peak values of 0.080×10^6 and

0.058×10^6 N m^{-1} appear at $\varphi = 60°$ and $90°$, respectively. Besides, the PPS/CF-based vibrator corresponding to $\varphi = 60°$ provides higher s_m, implying the probability to obtain larger torque than those to $\varphi = 45°$ and $90°$. Figures 4(g)–(i) illustrate the k–h relationships at $\varphi = 45°$, $60°$, and $90°$, respectively. The maximal k is 22.37% at $\varphi = 60°$, higher than the values at $\varphi = 45°$ and $90°$. Further, we explore the variation in f_0 against h at different φs. Figure 4(j) illustrates that, at $h = 2$ mm, f_0 equals 16.87 kHz, which is within the audible range and results in noise problem; and it gradually increases as the PPS/CF-based vibrator becomes thicker. Similarly, f_0 is
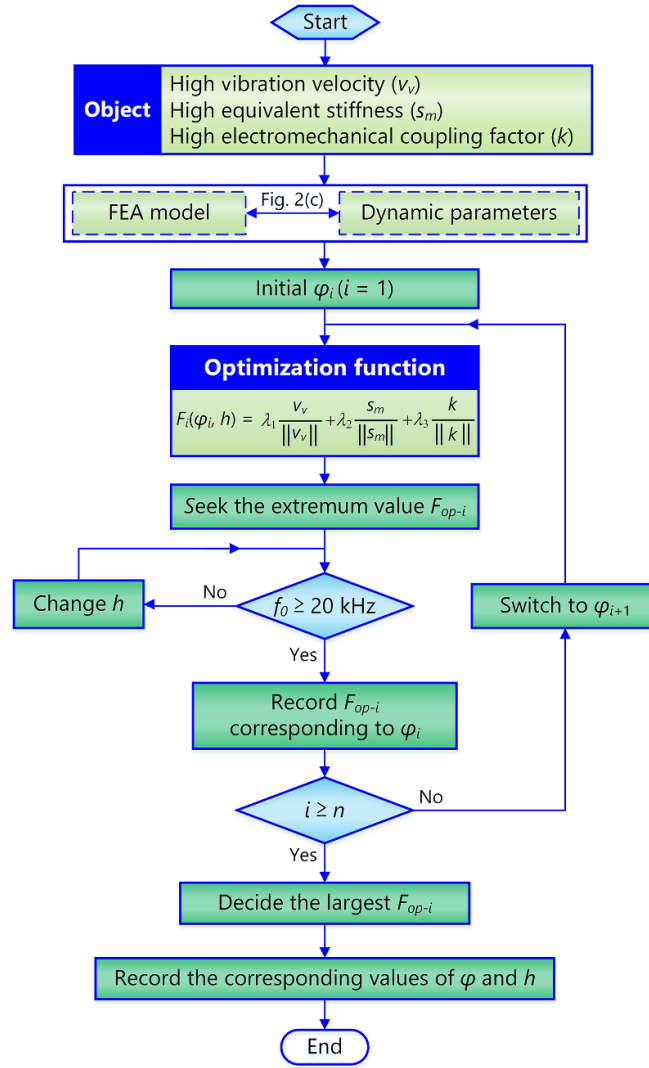
Figure 5. Flow chart of structural optimization of the PPS/CF-based vibrator.

lower than 20 kHz at $h = 2$ mm when φ is equal to 45° and 90° (see figures 4(k) and (l)). In addition to the tendencies, we obtained the function of each curve, which provided the basis for optimization.

2.4. Structural optimization

Since φ and h markedly affect v_v, s_m, k, and f_0, it is required to determine the optimal values. Figure 5 illustrates the optimizing procedures. Initially, the object is to increase v_v, s_m, and k, while the limitation is $f_0 \geqslant 20$ kHz. Subsequently, beginning with a certain value of φ_i [here, i is the integer, not larger than the number of φs (n)], an objective function is built as

$$F_i\left(\varphi_i, h\right) = \lambda_1 \frac{v_v}{\|v_v\|} + \lambda_2 \frac{s_m}{\|s_m\|} + \lambda_3 \frac{k}{\|k\|}. \quad (11)$$

Since we aim to increase the torque density and power density of polymer-based motors without excessively decreasing the speed, λ_1, λ_2, and λ_3 are set to 0.2, 0.4, and 0.4, respectively, and meanwhile, $\| \ \|$ means the maximal values obtained in simulation ($\|v_v\| = 134.4$ mm s^{-1}, $\|s_m\| = 0.080 \times 10^6$ N m^{-1}, $\|k\| = 22.4\%$). Followingly, by seeking the extremum value ($F_{op\text{-}i}$), we temporarily get an optimal value of h, and test whether the result satisfies the requirement of the resonance frequency. In the case of $f_0 < 20$ kHz, h is changed to an approaching value that not only produces a large F_i but also ensures $f_0 \geqslant 20$ kHz. Finally, φ_i is switched to φ_{i+1}, and $F_{op\text{-}i}$ are compared to $F_{op\text{-}i+1}$ to obtain the optimal φ and h. Note that, owing to the restriction in PPS/CF's fabrication, the number of φ should be finite for PPS/CF; this implies the suitability of the optimization method for the PPS/CF-based vibrators. Substituting the functions given in figure 5 into equation (11), we obtain that the optimal parameters are $\varphi = 60$ and $h = 4$ mm.
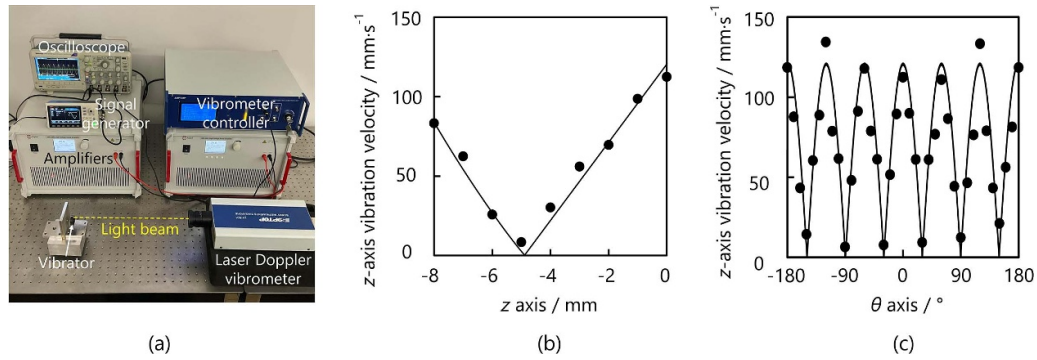
3. Vibration properties

First, various PPS/CF-based vibrators were fabricated by following the procedures given in figure 6. Originally, the carbon
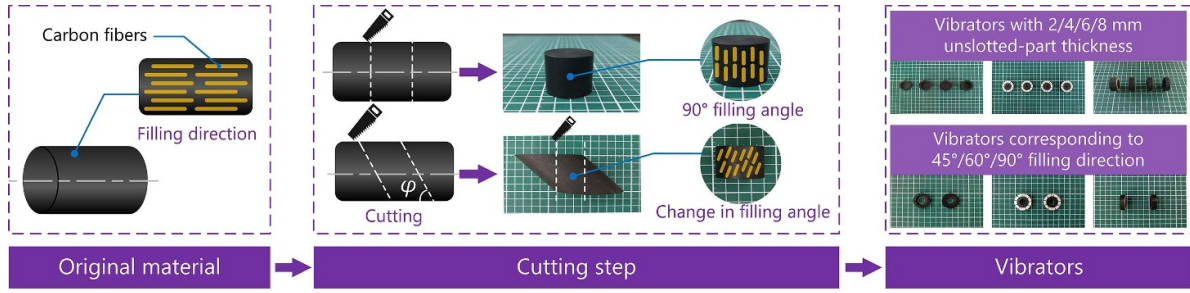
Figure 6. Fabrication process of the PPS/CF-based vibrators with various φs and hs.

Figure 7. Measurement of the vibration velocity distribution. (a) Testbed for measurement, and the vibration velocity distributions in (b) the z axis and (c) the θ axis. The curves represent the theoretical results, while the solid dots indicate the experimental results.

fibers are filled along the PPS bar's central axis. To make the vibrating body with $\varphi = 90°$, we vertically cut the PPS/CF bar and machined the ring-shaped vibrating body according to the configuration given in figure 2(a). While, to obtain the PPS/CF vibrating bodies with $\varphi = 45°$ and $60°$, we cut the PPS/CF bar with the tilting angle to make φ oblique to the bottom surface. For each φ, we fabricated a series of vibrating bodies as h ranged from 2 to 8 mm. After preparing the PPS/CF vibrating bodies, we bonded the PZT plates onto the vibrating bodies' back surface to form the vibrators. This approach permits the fabrication of the PPS/CF-based vibrators with varying φ and h.

Subsequently, the vibration velocity distributions of the PPS/CF-based vibrators were investigated to test whether the vibration was excited as predicted. As shown in figure 7(a), the vibrator was fixed to a base plate, and the longitudinal and bending vibration velocities were measured with in- and out-of-plane laser Doppler velocimeters (LV-IS01 and LV-S01, Sunny Optical Corp., Yuyao, China). The driving voltage was set to 50 V (note that, in this paper, the voltage and vibration velocity are expressed as zero-to-peak values) and the driving frequency was set to 24.42 kHz. Taking the PPS/CF-based vibrator with $\varphi = 60$ and $h = 4$ mm as an example, the z-axis vibration velocity distribution approached zero at $z = -5$ mm (see figure 7(b)) and the node's existence in the middle part of the vibrator indicated that the 1st longitudinal vibration was successfully excited in the z-axis. Figure 7(c) illustrates the z-axis vibration velocity distribution on the upper surface. The vibration velocities exhibited sinusoidal distribution with six nodes, indicating the excitation of the 3rd bending mode in the

θ axis. Besides, the longitudinal and bending vibration velocities had the maximal values of 112.4 and 134.4 mm s^{-1}, respectively.

Finally, to verify the excitation of elliptical motions, the vibration displacements on θ- and z-axes were measured by the laser Doppler velocimeter when the driving voltage and the working frequency were set to 250 V and 24.42 kHz, respectively. As shown in figure 8(a), the θ- and z-axis vibration displacements were 1.8 and 2.0 μm, respectively. Meanwhile, the θ-axis vibration displacement was in advance to the z-axis one by $\sim$40.92 μs, which corresponded to the phase of $\sim$90°. As illustrated in figure 8(b), the elliptical trajectory could be obtained by the superposition of the θ- and z-axis vibration displacements [49, 50]. Besides, the results coincided with the theoretical ones; this indicated the effectiveness of the proposed model. Besides, the bonding quality between the PZT plate and the PPS/CF vibrating body caused the slight deviation between the theoretical and experimental results since its effect on the damping coefficient was not clarified; this made it not easy to precisely set the damping coefficient during the simulation [51].
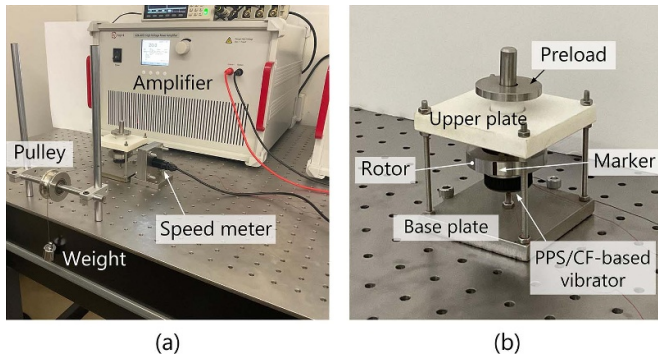
4. Motor performance

4.1. Experimental setup

Figure 9 illustrates the testbed for evaluating the performance of the PPS/CF-based motors. As shown in figure 9(a), the torque was estimated by pulling up weights, while the rotating speed was measured with a noncontact speed meter (HG200,
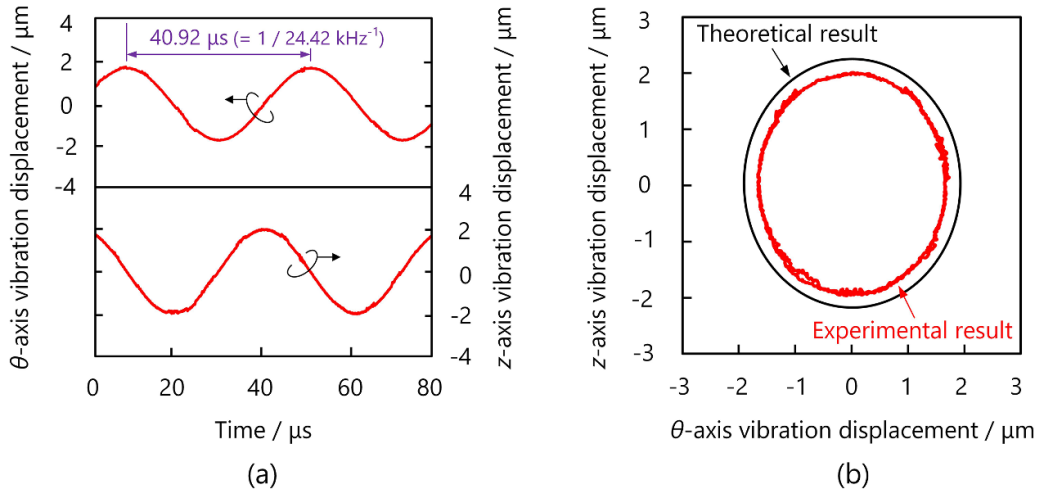
Figure 8. Verification of elliptical motion. (a) The θ- and z-axis vibration displacements in the time domain and (b) the formation of elliptical motion. The experimental results are given as the red curves, and the theoretical results obtained by the model are indicated as the black curve, respectively.

Figure 9. Testbed for assessing the performance. (a) The entire system and (b) the zoom-in view of the PPS/CF-based motor.

Aero-top Hitech Corp., Beijing, China). The voltages were applied with high-speed bipolar power amplifiers (ATA4052, Aigtek, Xi'an, China). The input power was recorded with high-frequency power meters (3332, Hioki E. E. Corp., Nagano, Japan). As shown in figure 9(b), the PPS/CF-based vibrator was fixed with a shaft connected to a stainless-steel base plate. The cylindrical outer surface of the shaft and the inner hole of the upper plate were both made by Teflon as its low friction coefficient facilitated the suppression of energy loss [39]. The rotor's bottom surface was directly in contact with the vibrator, while its upper part acted as a flywheel to obtain stable rotation. The stainless-steel disks were arranged onto the shaft's upper part to apply the preload to the rotor.

4.2. Movement characteristics

Initially, the movement characteristics of the PPS/CF-based motor with $\varphi = 60°$ and $h = 4$ mm were explored under the continuous operation. Figure 10(a) shows the output signal of the speed meter, where the high-level signals mean that the light beam emitted with the speed meter is reflected at the black mark while the low-level signals mean that

the light beam is irradiated onto the rotor's metal part. Note that only one mark was attached onto the circumferential surface. At the driving voltage of 200 V, there existed an interval of ~0.78 s between the adjacent low-level signals, while the interval increased to ~2.20 s when the voltage decreased to 100 V. Figure 10(b) plots the relationship between the round of rotation and the time period (adapted from figure 10(a)). It could be found in the fitting curve that, at 100 and 200 V, the rotation speeds were 27.2 and 76.5 r min^{-1}, respectively.

Figure 11(a) plots the variations in the motor's speed against f, where the peak speed exists at $f = 24.42$ kHz. Figure 11(b) shows that almost the same tendency can be found in the relationship between f and the vibration velocity. Figure 11(c) illustrates how the speed depends on α. Clearly, the speed increased when α was in the range from $-180°$ to $-80°$, reached its peak value in the counter-clockwise rotation at $\alpha = -80°$, and decreased as α changed from $-80°$ to $0°$. Meanwhile, the tendency corresponding to the clockwise rotation was consistent with that to the counter-clockwise rotation. Besides, at $\alpha = 100°$, the speed attained its maximal value of 99.3 r min^{-1} in the clockwise rotation. Figure 11(d) shows the variation in vibration velocity against α. Clearly, the values of α corresponding to the maximal vibration velocities approached those to the maximal speeds. Figure 11(e) shows the speeds as functions of V_0. Observably, the speed exhibited nearly linear enhancement as V_0 became larger because of increasing vibration velocity (see figure 11(f)). These results provide the basis for controlling the PPS/CF-based motor in further studies.
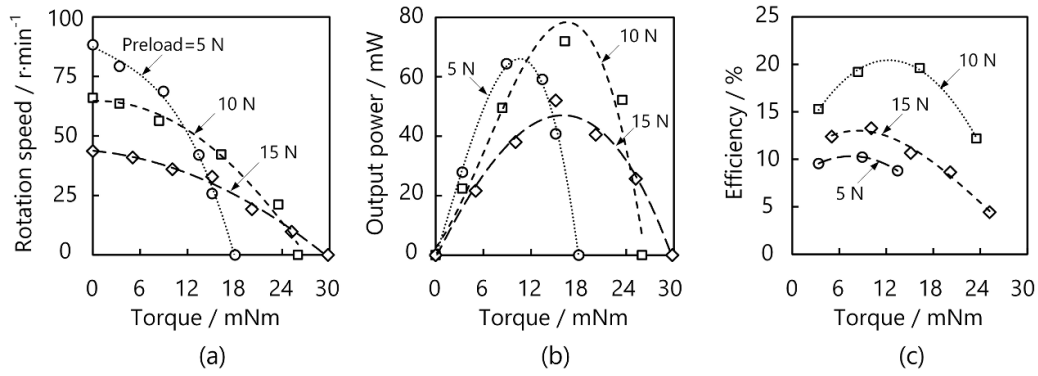
4.3. Load characteristics

Subsequently, the load characteristics of the PPS/CF-based motor with $\varphi = 60°$ and $h = 4$ mm were measured at $f = {\sim}24.42$ kHz, $\alpha = 100°$, and $V_0 = 250$ V. Figure 12(a) plots the no-load rotation speed as functions of the torque. At the preload of 5 N, the no-load rotation speed and maximal
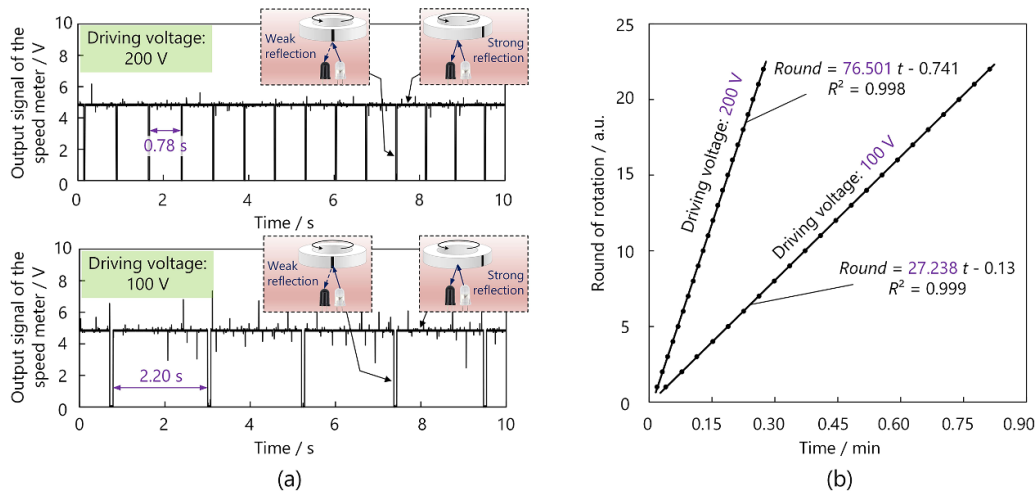
Figure 10. Measurement of the rotation round in the time domain. (a) The output signals of the speed meter at the driving voltages of 200 V and 100 V. (b) The round of rotation as functions of the time period.
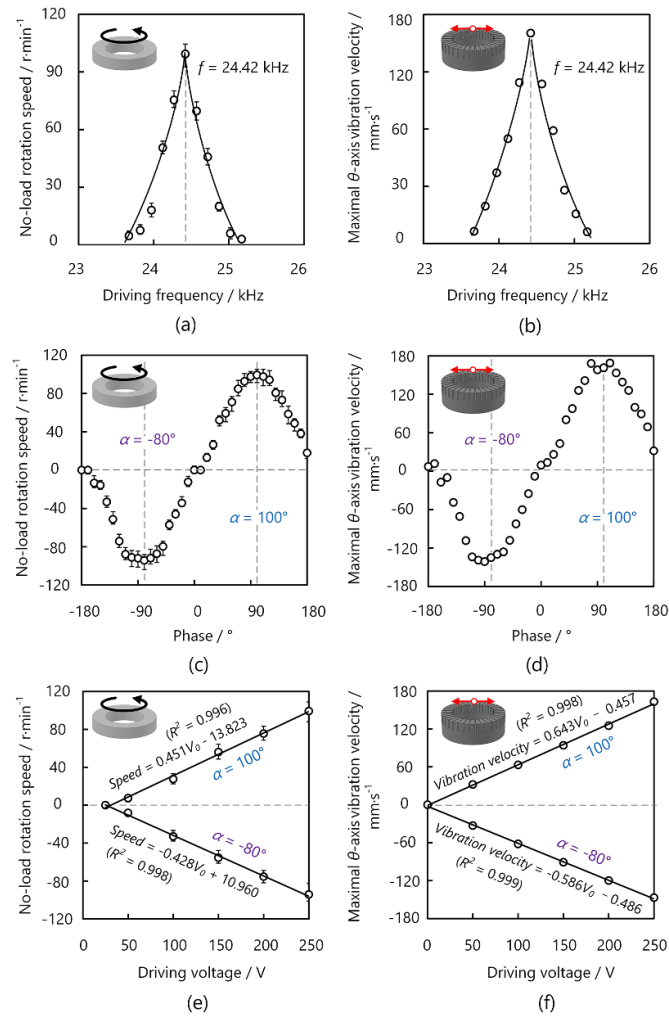
Figure 11. Variations in (a) the no-load rotation speed of the PPS/CF-based motor and (b) the maximal θ-axis vibration velocity obtained the vibrator against the driving frequency (other parameters: $V_0 = 250$ V and $\alpha = 100°$). Variations in (c) the no-load rotation speed and (d) the maximal θ-axis vibration velocity against the phase between two channels of excitation signals ($V_0 = 250$ V and $f = 24.42$ kHz). Variations in (e) the no-load rotation speed and (f) the maximal θ-axis vibration velocity against the driving voltage ($f = 24.42$ kHz and $\alpha = 100°/-80°$).

Figure 12. Load characteristics of the PPS/CF-based motor with φ = 60° and h = 4 mm. (a) Rotation speed, (b) output power, and (c) efficiency as functions of the torque at f = 24.42 kHz, α = 90°, and V0 = 250 V.

torque were 88.3 r min^{-1} and 18 mNm, respectively. As the preload increased to 10 N, the maximal torque of 26 mNm was obtained, while the no-load speed decreased to 66 r min^{-1}. When the preload increased to 15 N, the maximal torque reached 29.8 mNm. Figure 12(b) illustrates the variation in output power versus the torque. Clearly, the motor produced the maximal output power of 72 mW at the moderate torque of 18 mNm. Figure 12(c) shows how the efficiency depends on the torque. The efficiency corresponding to the preload of 10 N was higher than that to the preload of 5 N because the larger preload provided sufficient friction force [50, 51], and it also exceeded the efficiency corresponding to the preload of 15 N because excessive energy loss on the contact surface could be suppressed [50].

Followingly, the performances were compared among the PPS/CF-based motors with varying φ and h when the driving voltages were set to 250 V. Figure 13(a) illustrates how the maximal torque, maximal output power, maximal no-load speed depend on h at φ = 45°. The no-load speed reached 105.4 r min^{-1} at h = 2 mm and decreased monotonically as the vibrator became thicker, but the resonance frequency was smaller than 20 kHz. The maximal torque was 25.5 mNm at h = 4 mm. The maximal output power increased from 53.1 to 65.5 mW in h range from 2 to 6 mm. Figure 13(b) shows the variations in v_v, s_m, and k against h at φ = 45°. It could be found that the tendencies in v_v, s_m, and k were similar to those of the no-load speed, maximal torque, and maximal output power, respectively. In addition, the peak values of v_v, s_m, and k existed at h = 2, 4, and 6 mm, where the no-load speed, maximal torque, and maximal output power reached their peak values. As shown in figure 13(c), the no-load speeds, maximal torques, and maximal output powers corresponding to the PPS/CF-based motor with φ = 60° exhibited similar tendencies with those with φ = 45°. Meanwhile, the maximal torque and maximal output power were respectively 29.8 mNm and 75.4 mW for the motors with φ = 60°, higher than the values with φ = 45°; this should be, as shown in figure 13(d), caused by the larger s_m and k achieved at φ = 60°. As illustrated in figure 13(e), the motors with φ = 90° yielded the maximal torque and maximal output power of 27.7 mNm, and

60.5 mW, respectively, smaller than the values corresponding to φ = 60°; this should originate from relatively low v_v, s_m, and k (see figure 13(f)). By comparing the load characteristics, it can be found that the PPS/CF-based motor with φ = 60° and h = 4 mm is superior to the others in terms of the torque and output power; this infers the effectiveness of the optimization.

4.4. Performance comparison among polymer-based motors

Finally, the PPS/CF-based motor was compared with several previously-reported polymer-based rotary USMs. The results given in table 1 allow us to infer the following items.

(1) Compared to the PPS-based USM that utilizes only the 3rd bending modes [39], the PPS/CF-based motor produces relatively high torque density and high power density because it adopts the hybrid mode composed by the 3rd bending vibration in the θ axis and the 1st longitudinal vibration in the z axis [1, 9].

(2) The PPS/CF-based motor's torque density and power density are respectively 1.82 and 2.94 times the values of the PPS-based motor reported in [45] (though they both work in the hybrid mode); this should originate from the strong electromechanical coupling between the PPS/CF vibrating body and the PZT plate [9, 18, 19].

(3) By inserting a rigid layer (made of alumina) between the PPS vibrating body and the PZT plate [40], it is capable of enhancing the vibrator's equivalent stiffness and the triple-layered motor's torque density and power density; which are, however, smaller than the values of the PPS/CF-based motor because PPS/CF has lower density than alumina [47].

(4) The PPS/CF-based motor has a maximal torque of 29.8 mNm and a maximal output power of 72 mW. Moreover, the maximal torque density and power density reach 7.1 Nm kg^{-1} and 17.1 W kg^{-1}, respectively.
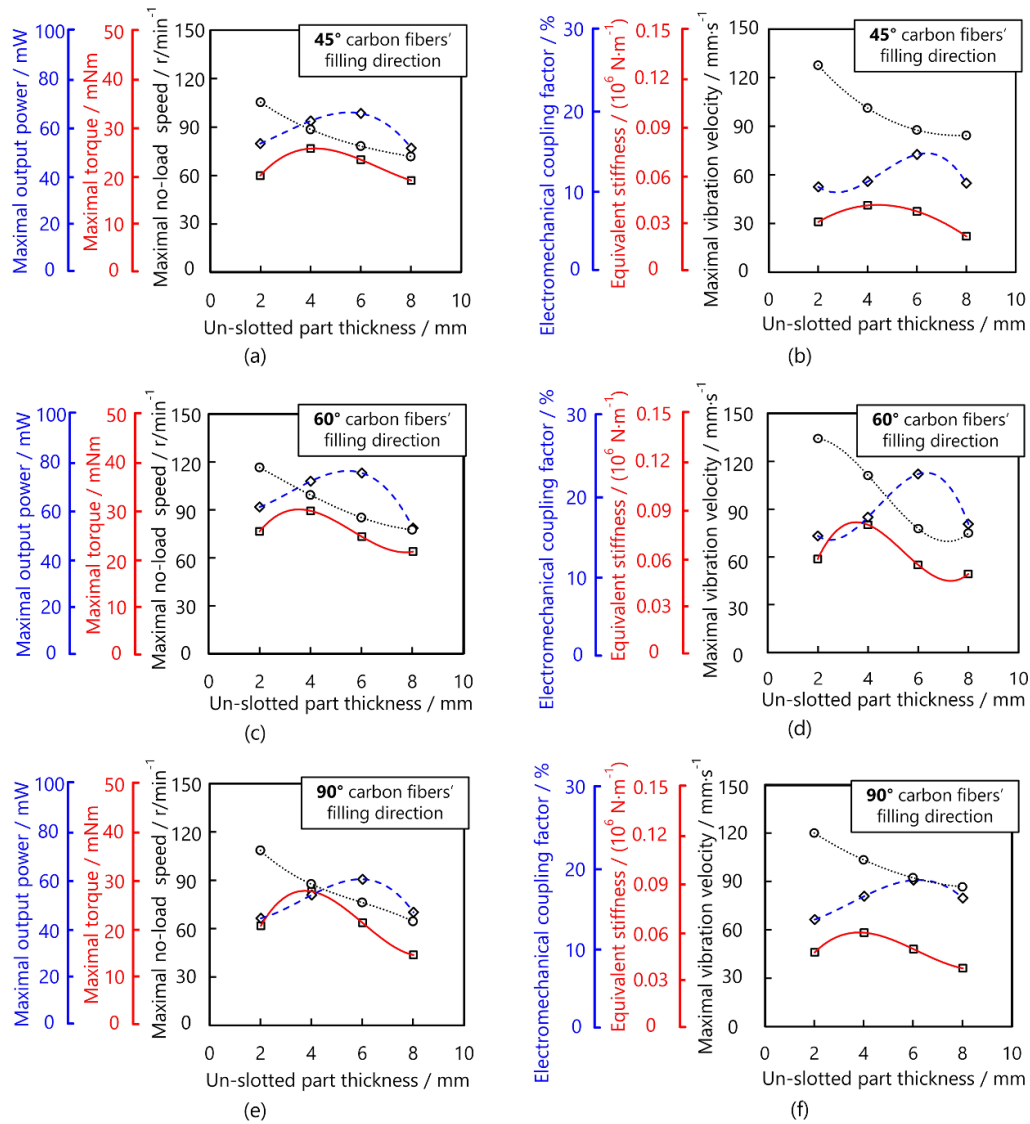
Figure 13. Comparison between the PPS/CF-based motors' performance at 250 V and the vibrators' dynamic parameters. (a) the maximal output power, maximal torque, no-load speed; and (b) electromechanical coupling factor, equivalent stiffness, maximal vibration velocity as functions of h at $\varphi = 45°$. (c) The maximal output power, maximal torque, no-load speed; and (d) electromechanical coupling factor, equivalent stiffness, maximal vibration velocity as functions of h at $\varphi = 60°$. (c) The maximal output power, maximal torque, no-load speed; and (b) electromechanical coupling factor, equivalent stiffness, maximal vibration velocity as functions of h at $\varphi = 90°$.

Table 1. Comparison between the PPS/CF-based motor and other polymer-based rotary USMs.

Performance	This study	[39]	[44]	[40]
Material of vibrating body	PPS/CF	PPS	PPS	PPS
Dimension (mm)	$\Phi30 \times 8.5$	$\Phi30 \times 9.5$	$\Phi30 \times 11.5$	$\Phi30 \times 6.5$
Vibration mode (in the θ axis)	3rd bending	3rd bending	3rd bending	3rd bending
(in the z axis)	1st longitudinal	—	1st longitudinal	—
Electromechanical coupling factor	22.4	6.9	11.8	17.9
Working frequency (kHz)	24.4	12.0	26.0	16.0
No-load rotation speed (r min^{-1})	99.3	45.8	114.6	85.0
Maximal torque (mNm)	29.8	1.4	9.5	15.2
Maximal output power (mW)	72.0	2.8	14.5	39.3
Torque density (Nm kg^{-1})	7.1	1.3	3.8	4.0
Power density (W kg^{-1})	17.1	2.5	5.8	10.3

5. Conclusion

This paper presents the proposal, design, and performance assessment of the PPS/CF-based motor. Through numerical analysis and experimental investigation, we have drawn the following conclusions.

(1) PPS/CF, a low-density functional polymer with anisotropically elastic moduli, was employed as the vibrating body to form rotary USMs, and the feasibility of this proposal was verified by testing the PPS/CF-based motor's performance.

(2) The dynamic model capable of setting the anisotropically elastic moduli with the changeable filling direction was established to estimate the PPS/CF-based vibrator's dynamic parameters (i.e. equivalent stiffness and electromechanical coupling factor). This model facilitated easy and quick design of the PPS/CF-based motors.

(3) Through structural optimization, $\varphi = 60°$ and $h = 4$ were estimated as the optimal parameters for the PPS/CF-based motor, where the no-load speed, maximal torque, and maximal output power of respectively 99.3 r min^{-1}, 29.8 mNm, and 72 mW were obtained.

(4) The PPS/CF-based motor yielded the torque density and power density of respectively 7.1 Nm kg^{-1} and 17.1 W kg^{-1}, exceeding the values of conventional polymer-based USMs.

These conclusions not only indicate that flexible usage of anisotropy of the elastic property of PPS/CF can enhance polymer-based motor's torque density and power density, but also pave a new way to design lightweight rotary USMs especially when the newly-developed materials with the anisotropically elastic property and good vibration characteristics are utilized as the vibrating bodies. To improve the polymer-based USMs' performance, we would like to focus on the optimization of the accessory components [49]. In addition, other polymer materials, such as glass-fiber-reinforced PPS [38], are worth testing to evaluate their suitability for USMs in the future.

Data availability statement

The data cannot be made publicly available upon publication because the cost of preparing, depositing and hosting the data would be prohibitive within the terms of this research project. The data that support the findings of this study are available upon reasonable request from the authors.

Acknowledgments

ORCID iDs

Jiang Wu ⬚ https://orcid.org/0000-0002-6899-5601
Zhaochun Ding ⬚ https://orcid.org/0000-0002-0014-8633

References

[1] Zhao J, Mu G, Dong H, Sun T and Grattan K T V 2022 Study of the velocity and direction of piezoelectric robot driven by traveling waves *IEEE Trans. Ind. Electron.* **70** 9260–9

[2] Tian X, Liu Y, Deng J, Wang L and Chen W 2020 A review on piezoelectric ultrasonic motors for the past decade: classification, operating principle, performance, and future work perspectives *Sens. Actuator* A **306** 111971

[3] Wang L, Wang R, Jia B, Zhao Z and Jin J 2022 Concept and electromechanical-coupling modeling of a torsional vibration excitation method *Int. J. Mech. Sci.* **236** 107709

[4] Liu R, Li X, Yu D, Cao T, Cao J, Wang B and Wu D 2022 A 3D printed sandwich-type piezoelectric motor with a surface texture *Rev. Sci. Instrum.* **93** 105003

[5] Ren W, Yang M, Chen L, Ma C and Yang L 2020 Mechanical optimization of a novel hollow traveling wave rotary ultrasonic motor *J. Intell. Mater. Syst. Struct.* **31** 1091–100

[6] Zhao J, Mu G, Dong H, Sun T and Grattan K T V 2022 Requirements for a transportation system based on ultrasonic waves using the measurement of spatial phase difference *Mech. Syst. Signal Process.* **168** 108708

[7] Deng J, Liu Y, Li J, Zhang S and Xie H 2022 Influence of multidirectional oscillations on output characteristics of inertial piezoelectric platform *IEEE/ASME Trans. Mechatronics* **27** 4122–31

[8] Zhang J, Yang L, Ma C, Ren W, Zhao C and Wang F 2019 Improving efficiency of traveling wave rotary ultrasonic motor by optimizing stator *Rev. Sci. Instrum.* **90** 056104

[9] Nakamura K 2012 *Ultrasonic Transducers: Materials and Design for Sensors, Actuators, and Medical Applications* (Cambridge: Woodhead Publishing Limited)

[10] Wang L, Jin J, Zhang H, Wang F and Jiang Z 2020 Theoretical analysis and experimental investigation on a novel self-moving linear piezoelectric stepping actuator *Mech. Syst. Signal Process.* **135** 106183

[11] Wang Y, Deng J, Zhang S, Li H, Chen W and Liu Y 2022 Design of a linear-rotary ultrasonic motor for optical focusing inspired by the bionic motion principles of the earthworms *Int. J. Smart Nano Mater.* **13** 346–65

[12] Qiu J, Yang Y, Hong X, Vasiljev P, Mazeika D and Borodinas S 2021 A disc-type high speed rotary ultrasonic motor with internal contact teeth *Appl. Sci.* **11** 2386

[13] Wu J, Wang L, Du F, Zhang G, Niu J, Rong X, Song R, Dong H, Zhao J and Li Y 2023 A two-DOF linear ultrasonic motor utilizing the actuating approach of longitudinal-traveling-wave/bending-standing-wave hybrid excitation *Int. J. Mech. Sci.* **248** 108223

[14] Ma X, Liu J, Deng J, Liu Q and Liu Y 2020 A rotary traveling wave ultrasonic motor with four groups of nested PZT ceramics: design and performance evaluation *IEEE Trans. Ultrason. Ferroelectr. Freq. Control* **67** 1462–9

[15] Yu H, Chen S, Liu J, Wang L and Hu J 2023 Development of a novel radial-torsional hollow ultrasonic motor and contact interface coating test *Ultrasonics* **131** 106950

[16] Jia B, Wang L, Wang R, Jin J, Zhao Z and Wu D 2021 A novel traveling wave piezoelectric actuated wheeled robot:

design, theoretical analysis, and experimental investigation *Smart Mater. Struct.* **30** 035016

[17] Chen D, Jin J, Zhang A, Wang L, Yu P and Liu R 2020 A novel U-shaped piezoelectric actuator for underwater robotic finger *Smart Mater. Struct.* **29** 125002

[18] Zhang A, Wang L, Jin J, Chen D, Liu R and Zhao H 2021 A novel piezoelectric actuated 2-DOF joint for underwater manipulator: design, simulation, and experimental investigation *Smart Mater. Struct.* **30** 105032

[19] Liu Y, Xu Z, Li X, Sun W and Huang H 2022 A high-performance stick-slip piezoelectric actuator achieved by using the double-stator cooperative motion mode (DCMM) *Mech. Syst. Signal Process.* **172** 108999

[20] Liu Z, Fu Q, Yang P, Dong Z, Zhang L and Yao Z 2023 Design and performance evaluation of a miniature I-shaped linear ultrasonic motor with two vibrators *Ultrasonics* **131** 106965

[21] Chen H, Nie R, Han W and Qiu J 2022 Improvement mechanism of energy conversion efficiency in ultrasonic motor with flexible rotor *Ultrasonics* **120** 106659

[22] Zhang J J, Diao W D, Fan K, Wang Z Q, Shi R Q and Feng Z H 2021 A miniature standing wave linear ultrasonic motor *Sens. Actuator* A **332** 113113

[23] Mustafa A and Morita T 2019 Efficiency optimization of rotary ultrasonic motors using extremum seeking control with current feedback *Sens. Actuator* A **289** 26–33

[24] Li X, Kan C, Cheng Y, Chen Z and Ren T 2020 Performance evaluation of a bimodal standing-wave ultrasonic motor considering nonlinear electroelasticity: modeling and experimental validation *Mech. Syst. Signal Process.* **141** 106475

[25] Zhao G, Wu C, Zhang L, Song J and Ding Q 2018 Friction and wear behavior of PI and PTFE composites for ultrasonic motors *Polym. Adv. Technol.* **29** 1487–96

[26] Zhang Y, Fu Y, Hua X, Quan L and Qu J 2020 Wear debris of friction materials for linear standing-wave ultrasonic motors: theory and experiments *Wear* **448** 203216

[27] Li J, Zeng S, Liu S, Zhou N and Qing T 2020 Tribological properties of textured stator and PTFE-based material in travelling wave ultrasonic motors *Friction* **8** 301–10

[28] Li S, Zhang N, Yang Z, Li X, Zhao G, Wang T, Wang Q and Zhang X 2019 Tailoring friction interface with surface texture for high-performance ultrasonic motor friction materials *Tribol. Int.* **136** 412–20

[29] Li H, Deng J and Liu Y 2023 Experimental research on the evolution characteristics of a bending hybrid ultrasonic motor during long-time operation *Ultrasonics* **131** 106957

[30] Qiu W, Mizuno Y, Adachi K and Nakamura K 2018 Ultrasonic motor performance influenced by lubricant properties *Sens. Actuator* A **282** 183–91

[31] Doshida Y, Tamura H and Tanaka S 2019 High-power properties of crystal-oriented $(Sr,Ca)_2NaNb_5O_{15}$ piezoelectric ceramics and their application to ultrasonic motors *Jpn. J. Appl. Phys.* **58** SGGA07

[32] Xin X, Yu Y, Wu J, Gao X, Li Z, Yi X, Chen W and Dong S 2020 A ring-shaped linear ultrasonic motor based on PSN-PMS-PZT ceramic *Sens. Actuator* A **309** 112036

[33] Lv Q, Yao Z, Jin Y and Liu B 2022 Wear evaluation model of a linear piezoelectric ultrasonic motor considering temperature effect *Ultrasonics* **126** 106822

[34] Lu D, Lin Q, Chen B, Jiang C and Hu X 2020 A single-modal linear ultrasonic motor based on multi vibration modes of PZT ceramics *Ultrasonics* **107** 106158

[35] He J, Chen Y, Cao B, Li X, Yang T, Hu Z, Ran L and Zhou W 2023 Traveling wave distortion of MEMS ultrasonic motor induced by anisotropic elasticity *Mech. Syst. Signal Process.* **189** 110083

[36] Ding Q, Zhao G, Peng H, Zhang Y and Li H 2014 Properties of carbon fiber reinforced poly(vinylidene fluoride)-based friction materials of ultrasonic motors *Polym. Compos.* **37** 547–52

[37] Qu J, Zhang Y, Tian X and Li J 2015 Wear behavior of filled polymers for ultrasonic motor in vacuum environments *Wear* **322** 108–16

[38] Wu J, Mizuno Y and Nakamura K 2019 Enhancement in mechanical quality factors of poly phenylene sulfide under high-amplitude ultrasonic vibration through thermal annealing *Ultrasonics* **91** 52–61

[39] Wu J, Mizuno Y and Nakamura K 2017 Structural parameter study on polymer-based ultrasonic motor *Smart Mater. Struct.* **26** 115022

[40] Wu J, Mizuno Y and Nakamura K 2018 Ultrasonic motors with poly phenylene sulfide/alumina/PZT triple-layered vibrators *Sens. Actuator* A **284** 158–67

[41] Chen G, Mohanty A K and Misra M 2021 Progress in research and applications of polyphenylene sulfide blends and composites with carbons *Composites* B **209** 108553

[42] TORAY Corporation Carbon fiber reinforced thermoplastic | information | TORAY resin products | TORAY (available at: www.plastics.toray/ja/products/torayca/) (Accessed 24 March 2023)

[43] Ding Z, Wei W, Wang K and Liu Y 2022 An ultrasonic motor using a carbon-fiber-reinforced/poly-phenylene-sulfide-based vibrator with bending/longitudinal modes *Micromachines* **13** 517

[44] Wu J, Mizuno Y and Nakamura K 2018 Polymer-based ultrasonic motors utilizing high-order vibration modes *IEEE/ASME Trans. Mechatronics* **23** 788–99

[45] Wu J, Mizuno Y and Nakamura K 2021 A rotary ultrasonic motor operating in torsional/bending modes with high torque density and high power density *IEEE Trans. Ind. Electron.* **68** 6109–20

[46] Campbell J J and Jones W R 1970 Propagation of surface waves at the boundary between a piezoelectric crystal and a fluid medium *IEEE Trans. Sonics Ultrason.* **17** 71–76

[47] Slabki M, Wu J, Weber M, Breckner P, Isaia D, Nakamura K and Koruza J 2019 Anisotropy of the high-power piezoelectric properties of $Pb(Zr,Ti)O_3$ *J. Am. Ceram. Soc.* **102** 6008–17

[48] Wu J, Mizuno Y, Tabaru M and Nakamura K 2016 Measurement of mechanical quality factors of polymers in flexural vibration for high-power ultrasonic application *Ultrasonics* **69** 74–82

[49] Zhang S, Zhao H, Ma X, Deng J and Liu Y 2023 A 3-DOF piezoelectric micromanipulator based on symmetric and antisymmetric bending of a cross-shaped beam *IEEE Trans. Ind. Electron.* **70** 8264–75

[50] Xu Z, Huang H and Dong J 2020 A stick-slip piezoelectric actuator with measurable contact force *Mech. Syst. Signal Process.* **144** 106881

[51] Mu G, Zhao J, Dong H, Wu J, Grattan K T V and Sun T 2021 Structural parameter study of dual transducer-type ultrasonic levitation-based transportation system *Smart Mater. Struct.* **30** 045009